HHS Public Access

Author manuscript

*Adv Mater*. Author manuscript; available in PMC 2021 August 01.

Published in final edited form as:

*Adv Mater*. 2020 August ; 32(33): e2002611. doi:10.1002/adma.202002611.

# Bioactive tissue derived nanocomposite hydrogel for permanent arterial embolization and enhanced vascular healing

**Jingjie Hu**,
Division of Vascular & Interventional Radiology, Minimally Invasive Therapeutics Laboratory, Mayo Clinic, 13400 East Shea Blvd., Scottsdale, Arizona 85259, USA

**Izzet Altun**,
Division of Vascular & Interventional Radiology, Minimally Invasive Therapeutics Laboratory, Mayo Clinic, 13400 East Shea Blvd., Scottsdale, Arizona 85259, USA

**Zefu Zhang**,
Division of Vascular & Interventional Radiology, Minimally Invasive Therapeutics Laboratory, Mayo Clinic, 13400 East Shea Blvd., Scottsdale, Arizona 85259, USA

**Hassan Albadawi**,
Division of Vascular & Interventional Radiology, Minimally Invasive Therapeutics Laboratory, Mayo Clinic, 13400 East Shea Blvd., Scottsdale, Arizona 85259, USA

**Marcela A. Salomao**,
Division of Anatomic Pathology & Laboratory Medicine, Department of Pathology, Mayo Clinic, 5777 East Mayo Blvd., Phoenix, Arizona 85054, USA

**Joseph L. Mayer**,
Division of Vascular & Interventional Radiology, Minimally Invasive Therapeutics Laboratory, Mayo Clinic, 13400 East Shea Blvd., Scottsdale, Arizona 85259, USA

**L.P. Madhubhani P. Hemachandra**,
Division of Vascular & Interventional Radiology, Minimally Invasive Therapeutics Laboratory, Mayo Clinic, 13400 East Shea Blvd., Scottsdale, Arizona 85259, USA

**Suliman Rehman**,
Division of Vascular & Interventional Radiology, Minimally Invasive Therapeutics Laboratory, Mayo Clinic, 13400 East Shea Blvd., Scottsdale, Arizona 85259, USA

**Rahmi Oklu***
Division of Vascular & Interventional Radiology, Minimally Invasive Therapeutics Laboratory, Mayo Clinic, 13400 East Shea Blvd., Scottsdale, Arizona 85259, USA

*Corresponding Author: Oklu.Rahmi@mayo.edu.

Experimental Section
Experimental details are included in the Supporting Information.

Supporting Information
Supporting Information is available from the Wiley Online Library or from the author.

Conflict of Interest
Dr. Oklu is a Founder and CMO of a start-up based on shear-thinning embolic materials (Obsido, Inc.).

## Abstract

Transcatheter embolization is a minimally invasive procedure that uses embolic agents to intentionally block diseased or injured blood vessels for therapeutic purposes. Embolic agents in clinical practice are limited by recanalization, risk of non-target embolization, failure in coagulopathic patients, high cost, and toxicity. Here, a decellularized cardiac extracellular matrix (ECM) based nanocomposite hydrogel was developed to provide superior mechanical stability, catheter injectability, retrievability, antibacterial properties and biological activity to prevent recanalization. The embolic efficacy of the shear-thinning ECM based hydrogel was shown in a porcine survival model of embolization in the iliac artery and the renal artery. ECM based hydrogel promotes arterial vessel wall remodeling and a fibroinflammatory response while undergoing significant biodegradation such that only 25% of the embolic material remains at 14 days. With its unprecedented pro-regenerative, antibacterial properties coupled with favorable mechanical properties, and its superior performance in anticoagulated blood, ECM based hydrogel has the potential to be the next generation biofunctional embolic agent that can successfully treat a wide range of vascular diseases.

## Table of Contents (ToC)

Biohybrid hydrogel comprised of cardiac-derived extracellular matrix (ECM) and nanoclay (NC) has been developed as a multifunctional embolic biomaterial that offers both biological activity and mechanical support necessary for successful arterial embolization. The shear-thinning ECM-NC hydrogel exhibits excellent transcatheter injectability, retrievability, and pro-angiogenic characteristics to serve as a catheter-directed bioactive embolic agent for the treatment of a variety of vascular diseases.

### Keywords

embolization; transcatheter delivery; decellularized extracellular matrix; hybrid nanocomposite hydrogel; vascular remodeling

Transarterial embolization (TAE) is a minimally invasive procedure to selectively deliver embolic agents into arteries to occlude diseased or injured vasculature for therapeutic intent; it is considered as the first-line therapy for most gastrointestinal tract bleeding and unresectable hepatocellular tumors.[1–3] Compared to invasive open surgeries, TAE offers a safe and efficient approach to control bleeding with better clinical outcomes and lower costs and has become a mainstay in treating many vascular diseases, including hemorrhage, aneurysms, vascular malformations, and hypervascular tumors.[2, 4–7] During TAE, a catheter is navigated through the vasculature under the guidance of X-ray fluoroscopy, and embolic agents are delivered to occlude the targeted vessels.[8] A variety of embolic agents such as coils, beads, and liquid embolics are currently used in the clinic; however, their effectiveness is limited by high cost, recanalization, toxicity, risk of non-specific embolization and stroke.[9–11] In particular, the versatility of embolization poses a major challenge in developing embolic agents, primarily due to a wide range of target vessel sizes (from 5–10 μm diameter capillaries to 1–2 cm diameter arteries) and architecture of the blood vessels (e.g., aneurysms versus vascular malformations) to be embolized or the type of

embolization required (e.g., permanent versus temporary).[12] For example, coils are commonly used solid embolic agents for the treatment of focal vascular conditions such as aneurysms and bleeding since they are intended to stay at the site of injury. However, liquid embolic agents such as Onyx (Medtronic, USA) are intended to travel distally from the site of release to penetrate finer vasculature, but they are associated with toxicity resulting from organic solvents.[2] Moreover, the mismatch between the sizes of embolic agents and targeted vessels can give rise to numerous complications during embolization, such as non-target embolization, recurrent hemorrhage, and organ ischemia.[13, 14] Therefore, it is of great importance to develop innovative strategies and new embolic agents with the ability to be adaptable to unique cases presented by each patient, possess desirable mechanical, radiopaque, and biological properties for effective embolization treatment, while also minimizing collateral injury to adjacent tissues.[2] To overcome the drawbacks of current embolic agents, strategic design of malleable hydrogels may offer significant advantages over both solid and liquid embolic agents used in the clinic today. Such hydrogels could be delivered using any catheter; they would form an impenetrable solid cast of various vessel geometries and sizes, avoiding embolization failure and recurrent bleeding, and provide the versatility that cannot be achieved by clinically used embolic agents. In addition, embolic agents used today merely lead to occlusion; next-generation embolic agents should also offer the flexibility to deliver therapeutics, including cells, drugs, gene therapy, and viral-vectors.

Injectable decellularized extracellular matrix (ECM) hydrogels provide an unparalleled therapeutic platform for minimally-invasive procedures in regenerative medicine and tissue engineering, such as tissue repair and organ replacement.[15] Mainly comprised of polysaccharides, including glycosaminoglycans and hyaluronic acid and fibrous proteins including, collagen, elastin, fibronectin, and laminin, ECM offers a highly dynamic microenvironment providing biomechanical and biochemical cues for tissue morphogenesis and homeostasis.[16–18] Decellularized ECMs from a variety of tissues have been used to make needle-based injectable hydrogels;[19, 20] however, only porcine-derived cardiac ECM hydrogels obtained from the left ventricle of the heart has advanced into a clinical trial to treat myocardial infarction.[21] Studies have shown that cardiac ECM hydrogels can promote muscle regeneration, facilitate vascularization, and modulate macrophage polarization towards tissue healing without hemocompatibility issues in vivo.[21, 22] These properties suggest that cardiac ECM hydrogels are biocompatible and regenerative, which can be highly beneficial for the remodeling of embolized vessels where ingrowth of connective tissue is desired for permanent vessel occlusion. Furthermore, cardiac ECM hydrogel can undergo sol-gel transition at body temperature, and such a gelation effect may benefit embolotherapy as a result of improved gel stability at targeted sites.[19] It is also naturally shear-thinning, which is desired for transcatheter-based delivery.[19] Despite these advantages, injectable cardiac ECM hydrogel still suffers from poor mechanical properties (usually with modulus less than 10 Pa) and a rapid degradation profile.[19] These hinder its clinical value; the ability to withstand physiologic pressures inside an artery and remain structurally intact throughout the treatment period are critical for an effective embolic agent. Hence, the combination of tissue-derived ECM with synthetic components is required to generate biohybrid materials with strength and resistance to fragmentation while also maintaining ECM's natural bioactivity.[18] To date, ECM based materials have not been

investigated for embolotherapy in TAE, where catheters longer than 100 cm with inner diameter as small as 600 μm are commonly used.

Here, we developed a unique class of ECM derived biohybrid nanocomposites to be used as multifunctional embolic agents. In order to overcome the limitations of currently used embolic agents, we have engineered novel nanocomposite gels comprised of decellularized ECM from the left ventricle of the porcine heart and laponite nanoclay (NC). Synthetic NCs are highly charged nanodisks with positive charges along the rim and negative charges at the faces. This anisotropic charge distribution endows NC the ability to form self-assembled structures with antimicrobial properties.[23, 24] By combining NC with ECM, we have significantly increased the mechanical strength and antibacterial characteristics of the hydrogel. The design of ECM-NC hybrid nanocomposites integrated the biochemical and biomechanical cues from ECM and the mechanical strength from synthetic NC to promote constructive remodeling in embolization as explored in a porcine model (Schematic 1). The bioactive ECM-NC hydrogel enabled wide tunability providing a platform technology for next-generation in vivo embolic agents to treat a broad range of vascular diseases.

First, we produced the cardiac ECM from the left ventricle of porcine hearts and characterized its microstructure and composition. To achieve this, the left ventricle was isolated, dissected into small pieces, decellularized and lyophilized (Figure 1A). Decellularization was confirmed by staining for cells and nuclei with hematoxylin and eosin stain (H&E) and DAPI (Figure 1B). Immunohistochemistry was also performed to confirm the preservation and structural integrity of collagen-I, fibronectin, and laminin after the decellularization process (Figure 1B). These structural proteins have been shown to promote cell adhesion, migration, and proliferation for functional repair and tissue regeneration.[25] Scanning electron microscopy (SEM) revealed the surface morphology of the decellularized cardiac tissue, showing its porous structure, compared to intact tissue (Figure 1B). Next, the decellularized extracellular matrix was digested with pepsin. The solubilized matrix was neutralized with NaOH forming the ECM solution, which was subsequently mixed with NC to create the ECM-NC hydrogel. The ECM solution underwent a sol-gel transition at 37 °C and showed mesh-like microarchitecture (Figure 1C). The DNA content of ECM was reduced by more than 98% ($p<0.0001$) compared to the native tissue and further confirmed that the decellularization process was complete, which is essential since cellular remnants such as DNA may provoke immunological reactions (Figure 1D).

The chemical composition of ECM was assessed by Fourier-transform infrared spectroscopy (FTIR), while protein composition was analyzed by SDS-polyacrylamide gel electrophoresis (SDS-PAGE). FTIR spectra of ECMs obtained from three different pigs revealed consistent amide bands. SDS-PAGE of the same ECMs and pooled ECM samples demonstrated consistent purity and protein composition (Figure 1F). Compared to rat-tail collagen-I, ECM showed bands at similar molecular weights; the protein composition of ECM mainly comprised of collagen proteins. These results suggested purity and homogeneity of the decellularized ECM isolated from the left ventricle of porcine heart, which was necessary for animal experiments.

The gelation kinetics of the ECM solution was examined by both turbidimetry and rheology. Turbidimetric measurement was used to assess the changes of optical density in the ECM solution at 37 °C, and the optical density was proportional to ECM concentration (Figure S1A, Supporting Information). The normalized gelation curve exhibited three distinct phases: a lag phase, an exponential growth phase, and a plateaued phase (Figure 1G). The gelation data was used to calculate the time needed to reach 50% of the maximum turbidity absorbance ($t_{1/2}$), the rate of gelation ($S$), and the lagging time ($t_{lag}$) (duration before gelation started) (Figure S1B, Supporting Information). Similar gelation kinetics was observed between 12 mg $mL^{-1}$ and 20 mg $mL^{-1}$ ECM solution (Figure S1C, S1D, and S1E, Supporting Information), whereas 9 mg $mL^{-1}$ ECM showed delayed gelation kinetics, possibly due to its lower concentration. In addition, time sweep measurement at 37 °C showed the $G'$ (storage modulus) of ECM was proportional to its concentration (Figure 1H), which was further confirmed in oscillatory amplitude sweep (Figure 1I). The gelation process resulted from entropy driven self-assembly process of collagen fibrils, resulting in stronger crosslinking and network strengthening.[19, 26] Therefore, 20 mg $mL^{-1}$ ECM solution was selected to make the ECM-NC gel due to its robust modulus enhancement upon increased temperature, as well as its high protein content and shear thinning properties (Figure 1J) for effective embolization.

Next, we designed and fabricated ECM-NC nanocomposites by mixing 20 mg $mL^{-1}$ ECM and 9 wt% Laponite NC (with an average hydrodynamic size of 7 nm) at predetermined ratios (Figure S2 and Table S1, Supporting Information). The gels were labeled as xECMyNC, where x was ECM percentage, and y represented NC percentage. To investigate the role of ECM on mechanical and biological properties of xECMyNC, a group of xECM4.5NC composites were produced at constant NC content of 4.5 wt%, and a final ECM amount ranging from 0 wt% (0 mg $mL^{-1}$) to 1 wt% (12 mg $mL^{-1}$). Rheological measurements were performed to assess the viscoelastic properties of ECM-NC gels, which all exhibited shear-thinning behavior (Figure 2A and Table S2, Supporting Information). It indicated that the xECM4.5NC composites experienced decreased viscosity upon applied shear to facilitate transcatheter injection. The $G'$ of xECM4.5NC was analyzed to understand the interaction between ECM and NC. Oscillatory time sweep measurements indicated that $G'$ was proportional to the ECM content with constant NC amount (Figure 2B and S3A, Supporting Information). Specifically, $G'$ of xECM4.5NC increased from 910 ± 4 Pa to 7327 ± 426 Pa ($p$<0.0001) at 37 °C with increasing ECM concentration from 0 to 1 wt %, suggesting enhanced mechanical strength and microstructure (Figure 2B). Furthermore, $G'$ value of 1ECM4.5NC 37 °C was 25 % higher compared to its value at 25 °C, whereas such enhancement was not evident in 0ECM4.5NC. The increase in G' of 1ECM4.5NC may attribute to the ECM gelation at 37 °C since 1ECM4.5NC possessed a final ECM concentration of 12 mg/mL that demonstrated thermally trigged gelation (Figure 1H). The yield stress also enhanced with the increasing amount of ECM from 76 ± 7 Pa (0ECM4.5NC) to 236 ± 22 Pa (1ECM4.5NC) ($p$<0.0001, Figure 2C, Figures S3B and S3C, Supporting Information), suggesting the gel's enhanced ability to withstand shear stress along a vasculature wall and increased resistance to material breakdown. Angular frequency sweep measurements showed that all xECM4.5NC gels exhibited $G'$ values approximately 7-50 times higher than $G''$ (loss modulus) values, suggesting the formation of stable

hydrogels (Figure 2D). In addition, xECM4.5NC nanocomposites were recoverable, with excellent self-healing properties under oscillating strains, mimicking intermittent injection, and deployment process during embolization procedure (Figure 2E). These results indicate that the ECM and NC could instantly form a stable network structure that is not disrupted under shear stress due to rapid, reversible electrostatic interactions.

Although the rheological properties correlate with the material's injectability, the injection force is the parameter that is directly related to physicians' experience.[2, 6] Therefore, compression tests were performed to measure the injection force that was required to pass the gel (loaded in a syringe) through a clinically used 110 cm, 2.8 French (F) microcatheter. The force-time plot included the plunger–stopper break-loose force, representing the force the physician needed to overcome to initiate the plunger movement, and the injection force, representing the force required to sustain the plunger movement (Figure 2F).[2] All xECM4.5NC gels generated a break-loose force of 18-27 N, representing forces that can be easily injected by hand during catheter delivery (Figure 2F and Figure S4, Supporting Information).[27] These results are significant because they indicate the simplicity and the speed of embolic delivery, a critical desirable feature for physician adoption, and reducing costs. Today, to deliver coils, often special catheters, wires, and devices to release the coil are required; these additional products increase the cost of the procedure, and they prolong the procedure time increasing exposure to X-ray.

To investigate cell viability in contact with xECM4.5NC nanocomposites, L929 mouse fibroblast cells were seeded over the gels. The amount of viable cells increased proportionally to the amount of ECM. Figure 2G demonstrates that 1ECM4.5NC (1 wt% ECM) exhibited the highest cell viability (136 ± 8%) ($p$<0.0001) compared to hydrogels containing less ECM. Since 1ECM4.5NC possessed the highest modulus, highest yield stress, and suitable injectability; this ECM hydrogel (EMH) was selected for further characterization.

To better understand the degree of physical crosslinking on gel properties, we prepared ECM-NC nanocomposites with varied ECM/NC ratios, while keeping the total solid amount (NC and ECM) constant at 5.5 wt% (Table S2). In addition to being shear-thinning (Figure S5A and S5B, Supporting Information), it is worth noting that $G'$ increased with increased ECM content and decreased NC amount (Figure S5C and S5D, Supporting Information). Over three-fold increase in $G'$ was observed between 0ECM5.5NC (1995 ± 84 Pa) and 1ECM4.5NC (7327 ± 426 Pa) ($p$<0.0001). These results suggested that the network's strength results from the interaction between the NC and ECM, in addition to the solid content that determined the strength of a hydrogel in the context of 0ECM4.5NC.[23, 28] Nanocomposites fabricated with a constant solid concentration of 5.5 wt % showed excellent mechanical stability, recoverability, and injectability (Figure S5E, S5F, S6A, and S6B, Supporting Information). These data demonstrated that by tuning the ratio between ECM and NC, we were able to achieve a wide range of nanocomposites with varying mechanical properties for a variety of in vitro and in vivo applications.

Radiopacity is of great importance for any embolic agents for real-time tracking under X-ray based fluoroscopy; this allows accurate deployment preventing non-target embolization.[2]

Here, a clinically used aqueous contrast agent, iohexol (350 mgI $mL^{-1}$), was incorporated into the xECM4.5NC to form a radiopaque hydrogel, xECM4.5NC-I, with a final iohexol concentration of 27 wt% (Table S3, Supporting Information). FTIR was used to confirm that ECM and iohexol were incorporated into the nanocomposite network (Figure 2H). The characteristic peaks of NC were observed in the final composites (1ECM4.5NC and 1ECM4.5NC-I). A shoulder at 535 $cm^{-1}$ appeared in 1ECM4.5NC-I, which may be due to the aromatic ring C-H out-of-plane bending from iohexol, and 1257 $cm^{-1}$ corresponds to C-N stretch in aromatic amine group in iohexol.[29] Negligible changes in peak positions along with similar FTIR patterns further revealed the noncovalent interactions between ECM, NC, and iohexol, suggesting the preservation of ECM protein complexes.

The effect of iohexol on the rheological property and bioactivity of nanocomposite hydrogels was further investigated. xECM4.5NC-I exhibited similar characteristics in mechanical properties compared to their radiolucent counterparts (Figure S7, Supporting Information). Specifically, the addition of contrast agent did not compromise the hydrogel's shear-thinning properties, embolic strength, or recoverability (Figure S7, Supporting Information). We generated radiopaque nanocomposites with $G'$ in the range of 1808 ± 176 Pa (0ECM4.5NC-I) to 8984 ± 73 Pa (1ECM4.5NC-I) ($p<0.0001$) (Figure S7D, Supporting Information). Overall, $G'$ of radiopaque hydrogels was increased due to the addition of iohexol. As a small molecule with multiple donor and acceptor sites, iohexol can form non-covalent crosslinks, such as hydrogen bonding and ionic interactions between ECM proteins thereby strengthening the overall nanocomposite structure (Figure 2I). The strengthening mechanism also resulted in higher injection forces (18 N-58 N) compared to their radiolucent counterparts, but still comfortably injectable by hand (Figure 2I, Figure S8A, and S8B, Supporting Information). It is interesting to note that for xECM4.5NC-I, an increased ECM concentration from 0.75 wt% to 1 wt% did not result in an increase in $G'$ at 25 °C, but an enhancement of $G'$ at 37 °C (Figure S6D, Supporting Information). This could be due to the saturation of electrostatic interactions with the addition of iohexol. Therefore, when ECM content increased from 0.75 wt% to 1 wt%, the degree of crosslinking did not increase at 25 °C, whereas self-assembly of collagen at 37 °C resulted in additional crosslinking that led to increased $G'$ of 1ECM4.5NC-I (Figures S7D, Supporting Information), suggesting its enhanced mechanical stability at physiological temperatures to support in vivo utilization. Therefore, we selected radiopaque 1ECM4.5NC-I, namely EMH-I, for further study.

To understand the influence of ECM and iohexol on the hierarchical structure of NC, SEM was used to investigate the microarchitecture of NC, EMH, and EMH-I (Figures S9, Supporting Information). A marked structural reinforcement was observed when ECM was integrated into NC. The matrix structure was further strengthened and became more organized with the addition of iohexol. Since both EMH and EMH-I had pH values around 8, collagen-I molecules, the major components of the ECM matrix,[25] were predicted to have both positive and negative charges along the chain,[30] thereby interacting with both edge and face of NC disks (Figure 2I). Compared to protein molecules (e.g., type A gelatin) carrying only positive charges that can interact purely with the faces of NC disks, the entangled conformation between ECM and NC offered a more compact and higher degree of hierarchical structures, therefore exhibiting significantly higher $G'$ compared to its gelatin

counterpart.[23] The mechanical strength of EMH and EMH-I was further confirmed with pressure displacement tests, which predicted the ability of EMH (65 ± 10 kPa) and EMH-I (119 ± 17 kPa) to withstand pressures much higher (over 4-fold and 7-fold, respectively) than physiological pressures (120 mmHg, equivalent to 16 kPa) (Figure 2J and S10, Supporting Information). Furthermore, EMH-I demonstrated the feasibility to be retrieved in vitro (Movie S1, Supporting Information). The retrievability endows EMH-I an important safety feature for rescuing non-target embolization and, for the first time, enabling temporary embolization. For example, the embolic agent could be removed from the internal iliac artery after treatment of pelvic hemorrhage avoiding buttock claudication.

In vitro tests revealed that both EMH and EMH-I were not cytotoxic. WST-1 assay was used as a qualitative evaluation of cytotoxicity by culturing L929 cells in hydrogel extracts for 24 hours at 37 °C, showing no toxicity of the gels (Figure 2K). Furthermore, Figure 2L shows that the optical density of E.coli bacteria suspension incubated with EMH and EMH-I was reduced 88.5 ± 3.6 % ($p$<0.0001) and 90.4 ± 0.7 % ($p$<0.0001), respectively, suggesting the significant antibacterial effect of both materials. The antibacterial properties of EMH and EMH-I suggest that embolization could also be performed in patients with bacteremia or sepsis.

To investigate the host response in vivo, we injected NC (control), EMH, and EMH-I into the dorsal subcutaneous tissue of Sprague-Dawley rats; the implants were excised 0, 3, 14, and 28 days after injection. Complete blood counts (CBC) at 0, 3, 14, and 28 days (Table S4 and Figure S11, Supporting Information) across all groups were within the normal range. All implants decreased approximately 50% in cross-sectional area at D28 compared to D3 on histology (NC 15 ± 2 $\mu m^2$ at D3 and 8 ± 1 $\mu m^2$ at D28, $p$=0.07; EMH 16 ± 4 $\mu m^2$ at D3 and 7 ± 1 $\mu m^2$ at D28, $p$=0.01; EMH-I 15 ± 4 $\mu m^2$ and D3 to 8 ± 2 $\mu m^2$ at D28, $p$=0.08) suggesting that all three materials degraded over time in vivo (Figure S12 and S13, Supporting Information). Histological analysis revealed that cellular infiltration into NC was significantly lower at day 3 and 14 compared to EMH and EMH-I ($p$<0.01) (Figure 3A, 3B and 3C). However, the total number of infiltrating cells was similar for these three gels at day 28 ($p$=0.6 between NC and EMH, $p$=0.6 between NC and EMH-I, $p$=0.9 between EMH and EMH-I) (Figure 3A and 3D). Analysis of Masson's trichrome staining for the thickness of the fibrotic capsule, defined as the dense collagen layer encapsulating the implant, is a standard measure of chronic inflammation to foreign materials following subcutaneous implantation (Figure 3E).[31, 32] The formation of a fibrotic capsule in response to foreign material is associated with upregulated fibroblast proliferation and activation, which leads to excess collagen deposition at the tissue-material interface.[32, 33] On analysis of the capsular thickness on histology indicated that the measured thickness of the capsule in EMH (116 ± 8 μm) and EMH-I (102 ± 8 μm) explants were decreased by 55 % ($p$<0.0001) and 60 % ($p$<0.0001), respectively, compared to NC (257 ± 26 μm) (Figure 3F). These results demonstrate that ECM can modulate chronic inflammatory events, and lead to faster host resolution of the tissue reaction and thinner capsule formation, which may be due to the downregulation of macrophage adhesion and activation.[34]

We further performed immunohistochemistry to assess inflammation and angiogenesis using antibodies against myeloperoxidase (MPO, marker of neutrophil granulocytes) and CD31

(endothelial cell marker) respectively. MPO positive cells were remarkably higher at early stage (D3) in EMH (1722 ± 33 $mm^{-2}$) ($p<0.0001$) and EMH-I (882 ± 197 $mm^{-2}$) ($p=0.3$) explants, compared to NC (146 ± 33 $mm^{-2}$) (Figure 3G). At D14, there was a marked increase in newly recruited inflammatory cells in EMH and EMH-I compared to D3 (Figure 3H). The physical cross-links in EMH and EMH-I can potentially be broken and displaced by migrating cells, resulting in enhanced cellular infiltration. By D28, inflammatory response subsided in EMH and EMH-I, indicating their biocompatibility (Figure 3H). Furthermore, CD31 quantification of the blood vessel density at the hydrogel-tissue interface revealed that EMH ($p=0.001$ for dermis and $p<0.0001$ for subcutaneous site compared to NC) and EMH-I ($p=0.04$ for dermis and $p<0.0001$ for subcutaneous site compared to NC) demonstrated a positive effect on angiogenesis in the long-term (D28) on both dermis (100 ± 40 and 83 ± 35 vessels $mm^{-2}$ for EMH and EMH-I, respectively) and subcutaneous sites (147 ± 49 and 126 ± 38 vessels $mm^{-2}$ for EMH and EMH-I, respectively), compared to NC (55 ± 23 and 60 ± 18 vessels $mm^{-2}$ for dermis and subcutaneous sites). This enhanced angiogenesis suggested pro-regenerative properties of EMH and EMH-I, and confirmed that iohexol did not compromise biocompatibility or bioactivity of the material ($p>0.05$, Figure 3J). Therefore, EMH-I was used in the subsequent large-animal studies since the presence of iohexol will allow its visibility under X-ray.

To demonstrate EMH-I's feasibility and applicability for potential clinical use, we delivered EMH-I through standard clinical catheters to explore its efficacy in arterial embolization in a porcine model. We aimed to investigate whether EMH-I can achieve instant embolization, remain at the site of release without migration or fragmentation avoiding non-target embolization, and whether it can enhance fibrosis of the arterial lumen to ensure that the occlusion is permanent. In addition, we explored the performance of EMH-I embolization in anticoagulated animals; pigs in the non-survival group received 10,000 units of heparin intravenously (IV) and the pigs in the survival group received daily anti-platelet therapy. The goal was to embolize an immediate branch of the aorta, i.e., a first-order artery; these arteries are larger in diameter, more challenging to achieve complete occlusion using coils today, have higher flow rates and higher pressures. We chose clinical scenarios that would be challenging to occlude with the embolization tools available today in order to demonstrate the superior performance of EMH-I.

From a carotid artery access, a 5 French catheter was delivered to the distal aorta, and contrast-enhanced digital subtraction angiography (DSA) was performed showing the iliac arteries (Figure 4A). Using a glidewire, the internal iliac artery (IIA) was catheterized with the 5 French catheter and embolization was performed (n=4); 1 mL syringe filled with EMH-I was connected to the catheter and, during real-time X-ray fluoroscopy, approximately a total of 3 mL of EMH-I was injected over 5-7 seconds creating an impenetrable cast of the artery. Subsequent DSA from the distal aorta immediately demonstrated the absence of flow in the IIA, showing complete occlusion (Figure 4B and 4C) despite having received IV heparin to achieve activated clotting time (ACT) values >300s.

A subset of the animals was allowed to survive 14 days (n=4); CT angiography (CTA) just prior to necropsy demonstrated persistent occlusion of the IIA without any evidence for non-

target embolization (Figure 4D). Flow to the hindlimb and flow distal to the embolized IIA were preserved from cross-pelvic collaterals; in addition, CT evaluation of the whole body by a board-certified radiologist revealed unremarkable findings with no evidence for lymphadenopathy or any other pathology. Consistent IIA embolization was achieved in all animals (Figure S15, S16 Supporting Information). Following necropsy, the IIA was harvested and further evaluated by high-resolution micro-computerized tomography (microCT) revealing material and tissue remodeling at D14. At D0, EMH-I uniformly occluded the artery with homogenous enhancement of the EMH in the arterial lumen (Figure 4E). At D14, the microCT enhancement pattern in the IIA lumen was heterogeneous (Figure 4E), suggesting EMH-I degradation and artery remodeling.

Following microCT imaging, the tissues were analyzed by histology and immunohistochemistry. Immunohistological staining of collagen-I, fibronectin, and laminin of the iliac artery at D0 confirmed the preservation of major ECM proteins in EMH-I in the embolized artery (Figure 4F and S14, Supporting Information). Histologic evaluation of arteries treated with EMH-I was performed by a board-certified pathologist. At D0, the ECM appeared as a pale pink amorphous material expanding and occluding the arterial lumen (Figure 4G). At D14, the arterial lumen remained entirely occluded, although the volume of ECM is reduced and partially replaced by a fibro-inflammatory process (Figure 4H). This process included infiltration of the arterial lumen by myofibroblasts, macrophages, and neutrophils, with early collagen deposition. Evaluation of the arterial wall by trichrome and elastic stains demonstrated preserved arterial wall thickness. Elastic stain showed disruption of elastic fibers at D14 (60 ± 5 %, $p<0.0001$) in the intima and media, but no significant injury to the smooth muscle layer was noted on trichrome stained slides (Figure 4G, 4H, and 4I). After 14 days, the normal structure of the arterial wall is disrupted by fibrosis (as demonstrated by the trichrome stain in Figure 4H) with breakdown of elastic fibers both in the internal elastic lamina and media layer (Elastin stain in Figure 4H). These changes are secondary to the inflammatory response elicited by the embolic material. A significant amount of proliferating cell nuclear antigen (PCNA) positive cells were also observed (2048 ± 262 $mm^{-2}$, $p<0.0001$), indicating that the bioactive EMH-I facilitated cell proliferation in the surrounding microenvironment (Figure 4J). Therefore, the histology evaluation performed 14 days following injection demonstrated that the arterial lumen remains completely occluded without evidence of recanalization. Morphologically, the hypercellular fibroinflammatory response observed in EMH-I samples appeared more robust than the response typically seen in an organizing thrombus. Subsequently, to determine the degradation rate of EMH-I within the arterial lumen, the volume of EMH-I was measured from reconstructed microCT images through segmentation by separating the material from connective tissue. By day 14, ECM-I in the arterial lumen was significantly reduced compared to day 0 samples (25 ± 5 % EMH-I remaining at D14; $p=0.0001$) (Figure 4K) and was replaced by non-enhancing fibrotic tissue.

To investigate whether the embolic material leads to micro-fragmentation, an end-organ artery such as the main renal artery of the kidney was embolized. Any fragmentation from the embolized main renal artery would be detected by high-resolution microCT imaging and by histology. In addition, any recanalization of the main renal artery would show contrast enhancement of the renal parenchyma by CTA imaging. From a carotid artery access, a 5

French catheter was used to catheterize one of the main renal arteries, and DSA was performed demonstrating the normal renal arterial anatomy (Figure 5A and S17, Supporting Information). From a distal renal artery position, approximately 2-3 mL of EMH-I was injected through the 5 French catheter causing immediate casting along the arterial lumen (Figure 5B). Subsequent DSA images from the aorta demonstrated the absence of flow in the embolized renal artery with no contrast-enhancement of the kidney despite the animals receiving anticoagulation (Figure 5C). A subset of these animals was allowed to survive 14 days (n=4). Prior to necropsy, contrast enhanced CTA was performed, demonstrating persistent occlusion of the embolized artery with no evidence for contrast enhancement of the renal parenchyma suggesting the absence of recanalization (Figure 5D and 5E, S17 and S18, Supporting Information). A significant reduction (~36%) in kidney volume was also detectable post-embolization at D14 (213 ± 15 $cm^3$ for non-embolized kidney, and 135 ± 20 $cm^3$ for embolized kidney, $p$=0.02) (Figure 5F). Following whole-body CT imaging, the embolized and the contralateral normal kidney were harvested (Figure 5G and 5H). These kidneys were further evaluated by microCT imaging, which revealed the absence of micro-emboli and complete occlusion of the renal artery (Figure S19, Supporting Information). On histology, there was no evidence of EMH-I in the cortex, suggesting that micro-emboli did not occur (Figure 5G and 5H). Histological analysis indicated the ability of EMH-I to penetrate vessel sizes down to 200 μm (Figure 5H). The thinning of renal capsule, the destruction of tubules and glomeruli, and the fibrotic tissue in the parenchyma at D14 all indicated the absence of blood flow and the loss of physiological function of the kidney (Figure 5G and 5H).[35]

In these minimally invasive embolization experiments, all pigs tolerated the embolization procedure without any signs of distress. Blood hematology and serum biochemistry results demonstrated the absence of any signs of infection and normal organ function, including renal and liver function at day 14 (Table S5, Supporting Information). Vital organs, including lung, liver, spleen, heart, brain, and lower limb, as shown in whole-body CT scans (Figure S20, Supporting Information), were unremarkable. There was no evidence for lymphadenopathy, pulmonary emboli, or stroke, suggesting that EMH-I did not traverse the capillary bed of the embolized artery. In this study, the pigs were survived to 14 days; to better understand long term embolic efficacy of EMH-I and its systemic response, experiments lasting 6 months to 1 year would be necessary.

In conclusion, we have developed a novel class of bioactive, tissue-derived, mechanically robust, and radiopaque ECM-based nanocomposite for vascular embolization. EMH-I has shear-thinning properties allowing it to be injected from a wide range of micro and standard clinical catheters for easy and rapid injection resulting in instant hemostasis. In comparison to embolic agents used today, EMH-I is a “one-size-fits-all” embolic agent that does not require additional wires, devices, or special catheters for use. EMH-I also has unique properties in that it is mechanically stable, achieving persistent occlusion without migration or fragmentation in first-order arteries. It is also antimicrobial and pro-regenerative. EMH-I achieved complete occlusion of the embolized arteries despite being anticoagulated; this is a desirable feature in an embolic agent as coils today fail because they rely on the bodies intrinsic ability to form a thrombus to occlude the coil mass inside the artery. These properties and its ease of use make the ECM-NC nanocomposite highly attractive for a wide

range of embolization applications, such as treatment of aneurysms and vascular malformations. The novel hybrid design of integrating tissue-based biological functions from ECM proteins and mechanical strength from synthetic nanoclay represents a new direction in the endovascular treatment of vascular diseases.

## Supplementary Material

Refer to Web version on PubMed Central for supplementary material.

## Acknowledgements

The authors gratefully acknowledge funding from the National Institutes of Health (R01HL140951, R01EB024403, and R01HL137193) and the Mayo Clinic.

## References

[1]. Shin JH, Korean J. Radiol 2012, 13, S31. [PubMed: 22563285]

[2]. Hu J, Albadawi H, Chong BW, Deipolyi AR, Sheth RA, Khademhosseini A, Oklu R, Adv. Mater 2019, 31, 1901071.

[3]. Idee JM, Guiu B, Critical Reviews in Oncology Hematology 2013, 88, 530.

[4]. Tarasconi A, Baiocchi GL, Pattonieri V, Perrone G, Abongwa HK, Molfino S, Portolani N, Sartelli M, Di Saverio S, Heyer A, Ansaloni L, Coccolini F, Catena F, World J. Emerg. Surg 2019, 14, 3. [PubMed: 30733822]

[5]. Zhou F, Chen LM, An QZ, Chen L, Wen Y, Fang F, Zhu W, Yi T, Sci. Rep 2016, 6.

[6]. Wang CY, Hu J, Sheth RA, Oklu R, Prog. Biomed. Eng 2020, 2, 012003.

[7]. Poursaid A, Jensen MM, Huo E, Ghandehari H, J. Controlled Release 2016, 240, 414.

[8]. Avery RK, Albadawi H, Akbari M, Zhang YS, Duggan MJ, Sahani DV, Olsen BD, Khademhosseini A, Oklu R, Sci. Transl. Med 2016, 8.

[9]. Lam D, Enright HA, Peters SKG, Moya ML, Soscia DA, Cadena J, Alvarado JA, Kulp KS, Wheeler EK, Fischer NO, J. Neurosci. Methods 2020, 329, 108460. [PubMed: 31626846]

[10]. Zhu Y, Zhang H, Zhang Y, Wu H, Wei L, Zhou G, Zhang Y, Deng L, Cheng Y, Li M, Santos HA, Cui W, Adv. Mater 2018, 0, 1805452.

[11]. Vaidya S, Tozer KR, Chen J, Seminars in interventional radiology 2008, 25, 204. [PubMed: 21326511]

[12]. Transcatheter Embolization and Therapy, 1st ed. (Eds: Kessel D, Ray C), Springer-Verlag, London, UK 2010

[13]. Chuang VP, Wallace S, Gianturco C, Soo CS, Am. J. Roentgenol 1981, 137, 809. [PubMed: 7027770]

[14]. Tummala RP, Chu RM, Madison MT, Myers M, Tubman D, Nussbaum ES, Neurosurgery 2001, 49, 1059. [PubMed: 11846898]

[15]. Liu M, Zeng X, Ma C, Yi H, Ali Z, Mou X, Li S, Deng Y, He N, Bone Res. 2017, 5, 17014. [PubMed: 28584674]

[16]. Frantz C, Stewart KM, Weaver VM, Cell Sci J. 2010, 123, 4195.

[17]. Afewerki S, Sheikhi A, Kannan S, Ahadian S, Khademhosseini A, Bioeng. Transl. Med 2019, 4, 96. [PubMed: 30680322]

[18]. Bracaglia LG, Fisher JP, Adv. Healthcare Mater 2015, 4, 2475.

[19]. Saldin LT, Cramer MC, Velankar SS, White LJ, Badylak SF, Acta Biomater. 2017, 49, 1. [PubMed: 27915024]

[20]. Bejleri D, Davis ME, Adv. Healthcare Mater 2019, 8, 1801217.

[21]. Traverse JH, Henry TD, Dib N, Patel AN, Pepine C, Schaer GL, DeQuach JA, Kinsey AM, Chamberlin P, Christman KL, JACC: Basic to Translational Science 2019, 4, 659. [PubMed: 31709316]

[22]. Duran P, Alperin M, Christman KL, in Decellularized Extracellular Matrix: Characterization, Fabrication and Applications, The Royal Society of Chemistry, 2020, 116.

[23]. Gaharwar AK, Avery RK, Assmann A, Paul A, McKinley GH, Khademhosseini A, Olsen BD, ACS Nano 2014, 8, 9833. [PubMed: 25221894]

[24]. Rawat K, Agarwal S, Tyagi A, Verma AK, Bohidar HB, Appl. Biochem. Biotechnol 2014, 174, 936. [PubMed: 24894661]

[25]. Keane TJ, Horejs C-M, Stevens MM, Adv. Drug Del. Rev 2018, 129, 407.

[26]. Wolf MT, Daly KA, Brennan-Pierce EP, Johnson SA, Carruthers CA, D'Amore A, Nagarkar SP, Velankar SS, Badylak SF, Biomaterials 2012, 33, 7028. [PubMed: 22789723]

[27]. Rungseevijitprapa W, Bodmeier R, Eur. J. Pharm. Sci 2009, 36, 524. [PubMed: 19124076]

[28]. Samimi Gharaie S, Dabiri MS, Akbari M, Polymers 2018, 10.

[29]. Liu Y, Ma Y, Zhao Y, Sun X, Gándara F, Furukawa H, Liu Z, Zhu H, Zhu C, Suenaga K, Oleynikov P, Alshammari AS, Zhang X, Terasaki O, Yaghi OM, Science 2016, 351, 365. [PubMed: 26798010]

[30]. Uquillas JA, Akkus O, Ann. Biomed. Eng 2012, 40, 1641. [PubMed: 22314838]

[31]. Anderson JM, Rodriguez A, Chang DT, Semin. Immunol 2008, 20, 86. [PubMed: 18162407]

[32]. Bridges AW, Whitmire RE, Singh N, Templeman KL, Babensee JE, Lyon LA, García AJ, J. Biomed. Mater. Res. A 2010, 94A, 252.

[33]. Rujitanaroj P.-o., Jao B, Yang J, Wang F, Anderson JM, Wang J, Chew SY, Acta Biomater. 2013, 9, 4513. [PubMed: 23036951]

[34]. Huleihel L, Dziki JL, Bartolacci JG, Rausch T, Scarritt ME, Cramer MC, Vorobyov T, LoPresti ST, Swineheart IT, White LJ, Brown BN, Badylak SF, Semin. Immunol 2017, 29, 2. [PubMed: 28736160]

[35]. Zhang YY, Gao HJ, Wang H, Xu ZY, Chen XW, Liu B, Shi Y, Lu Y, Wen LF, Li Y, Li ZS, Men YF, Feng XQ, Liu WG, Adv. Funct. Mater 2018, 28.

[36]. Johnson TD, Lin SY, Christman KL, Nanotechnology 2011, 22, 494015. [PubMed: 22101810]

[37]. I. O. f. Standardization, in ISO 10993-5, 2009.

[38]. Han L, Li P, Tang P, Wang X, Zhou T, Wang K, Ren F, Guo T, Lu X, Nanoscale 2019, 11, 15846. [PubMed: 31289795]

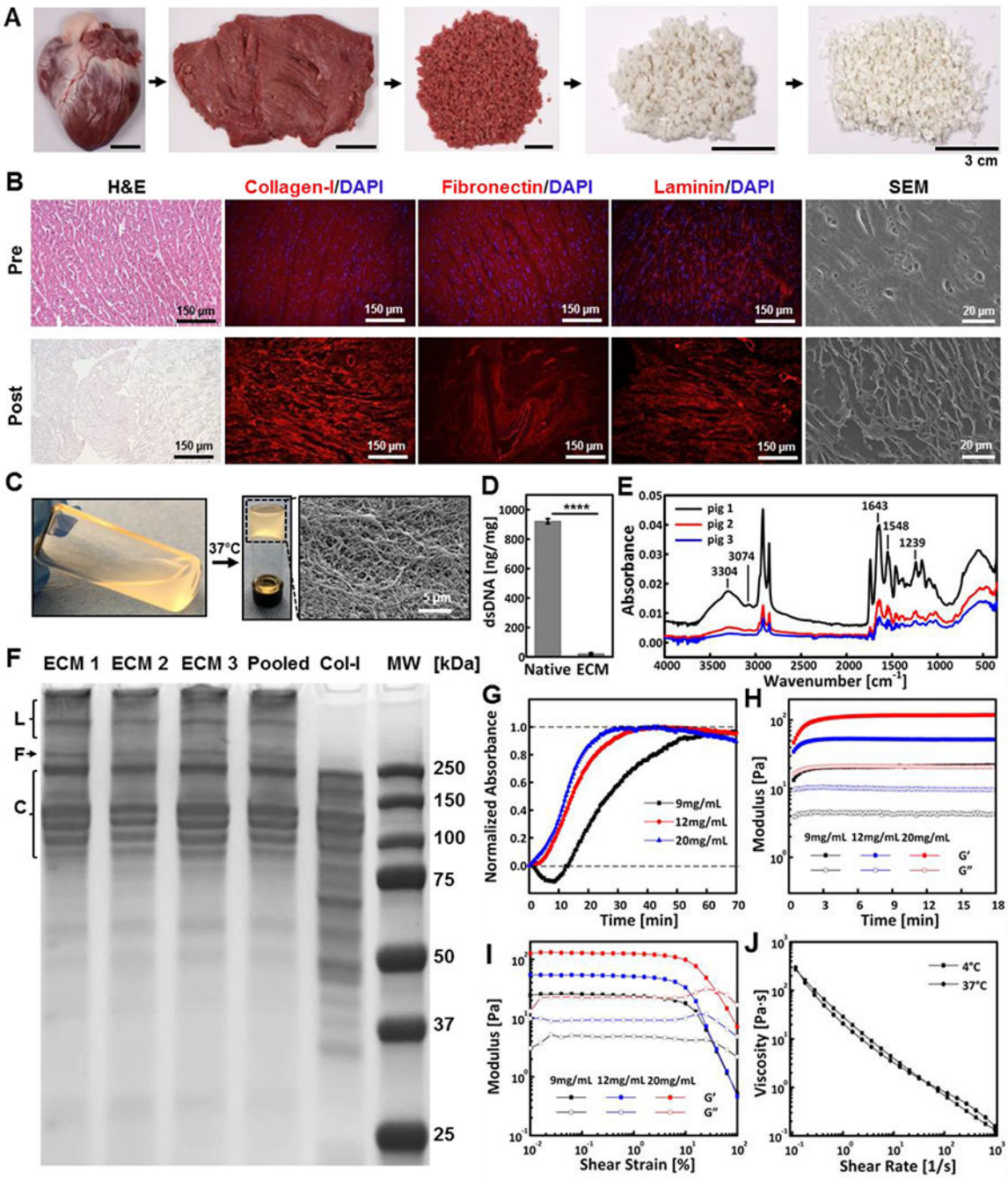


**Figure 1.**

ECM preparation and characterization. (A) Decellularized cardiac tissue preparation comprised of dissecting the left ventricle of the porcine heart, followed by decellularization and lyophilization. (B) Representative images of cardiac tissue characterization pre and post decellularization including H&E, immunostaining of collagen-I, fibronectin and laminin, and SEM. (C) Decellularized cardiac tissue being digested and neutralized to form ECM solution, which underwent sol-gel transition at 37 °C creating a nano-fibered mesh. (D) dsDNA amount in the native tissue and ECM, confirming successful decellularization. (E)

FTIR spectra of ECM samples prepared from three different pigs, showing composition consistency. (F) SDS-PAGE gel of ECM samples prepared from different porcine hearts (ECM1-ECM3) individually, pooled samples, and rat tail collagen-I protein (Col-I), showing consistency of protein composition in prepared ECMs with the major component being Col-I. Expected locations of laminin (L), fibronectin (F) and collagen-I bands (C) are labeled. (G) Representative turbidimetric gelation kinetics of ECMs at concentrations of 9, 12, and 20 mg $mL^{-1}$. (H) Gelation kinetics of ECMs at 37 °C measured by rheometry, showing concentration-dependent kinetics. (I) Representative $G'$ and $G''$ curves as a function of the amplitude of oscillatory shear strain measured for ECMs. (J) Shear rate sweep revealing the shear-thinning nature of ECM (20 mg $mL^{-1}$) at 4 °C and 37 °C. ****$p < 0.0001$. Each data point represents average ± standard deviation.

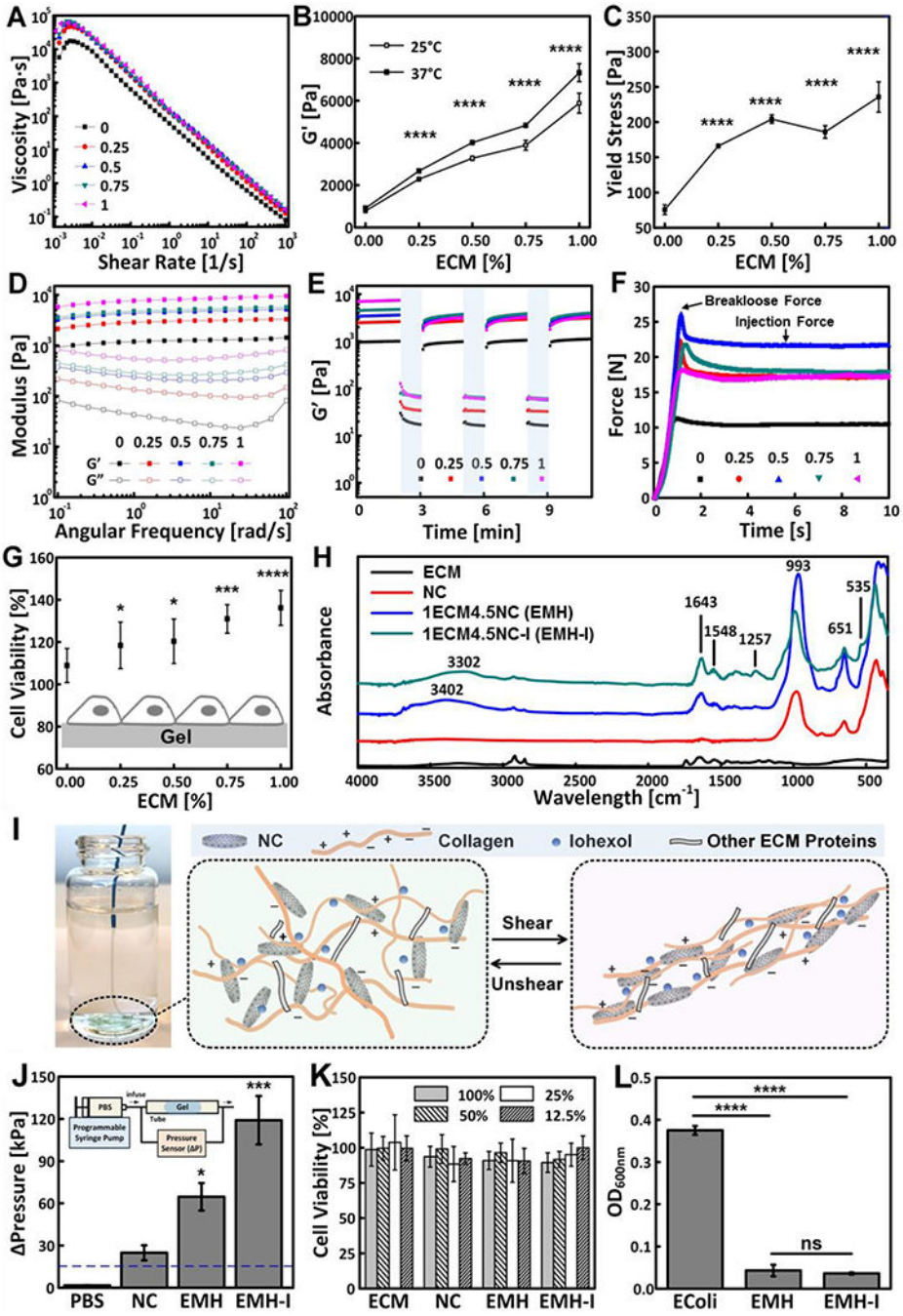


**Figure 2.**

Mechanical properties and biofunctionalities of ECM-NC nanocomposite hydrogels. Rheology of xECM4.5NC, as characterized by (A) Shear rate sweeps. (B) *G'* measured from oscillatory strain sweeps performed at 10 rad $s^{-1}$ (n=3). (C) Yield stress calculated from oscillatory strain sweeps (n=3). (D) Oscillatory frequency sweeps performed at 0.1 % strain; (E) Time sweep revealing recoverability of gels under alternating cycles between 2-minute low 0.1 % strain and 1-minute high 100 % strain at 10 rad $s^{-1}$. (F) Representative injection force curves, showing breakloose and injection forces. (G) Cell viability of L-929 fibroblasts

seeded directly on ECM gels 16 hours, showing enhanced cell viability with an increasing amount of ECM in the gels (n=8). (H) FTIR spectra of ECM, NC, EMH, and EMH-I, showing chemical composition. (I) EMH-I extruded from a 2.8 F catheter by manual injection and schematics showing interactions between ECM proteins, NC and iohexol network under shear. (J) The pressure required to displace control (PBS alone), NC, EMH, and EMH-I (n=3). Inset shows the schematics of tube-based setup for in vitro occlusion assessment. (K) Viability of L-929 cells after incubated with ECM, NC, EMH, and EMH-I extractions at different concentrations for 24 hours, showing no toxicity of the gels (n=12). (L) Antibacterial properties tested by measuring the optical density of *E.coli* suspensions that were cultured on EMH and EMH-I (n=8). Unless otherwise stated, all experiments on gels were performed at 37 °C. ns, not significant; $*p < 0.05$, $**p < 0.01$, $****p < 0.0001$. Each data point represents average ± standard deviation.

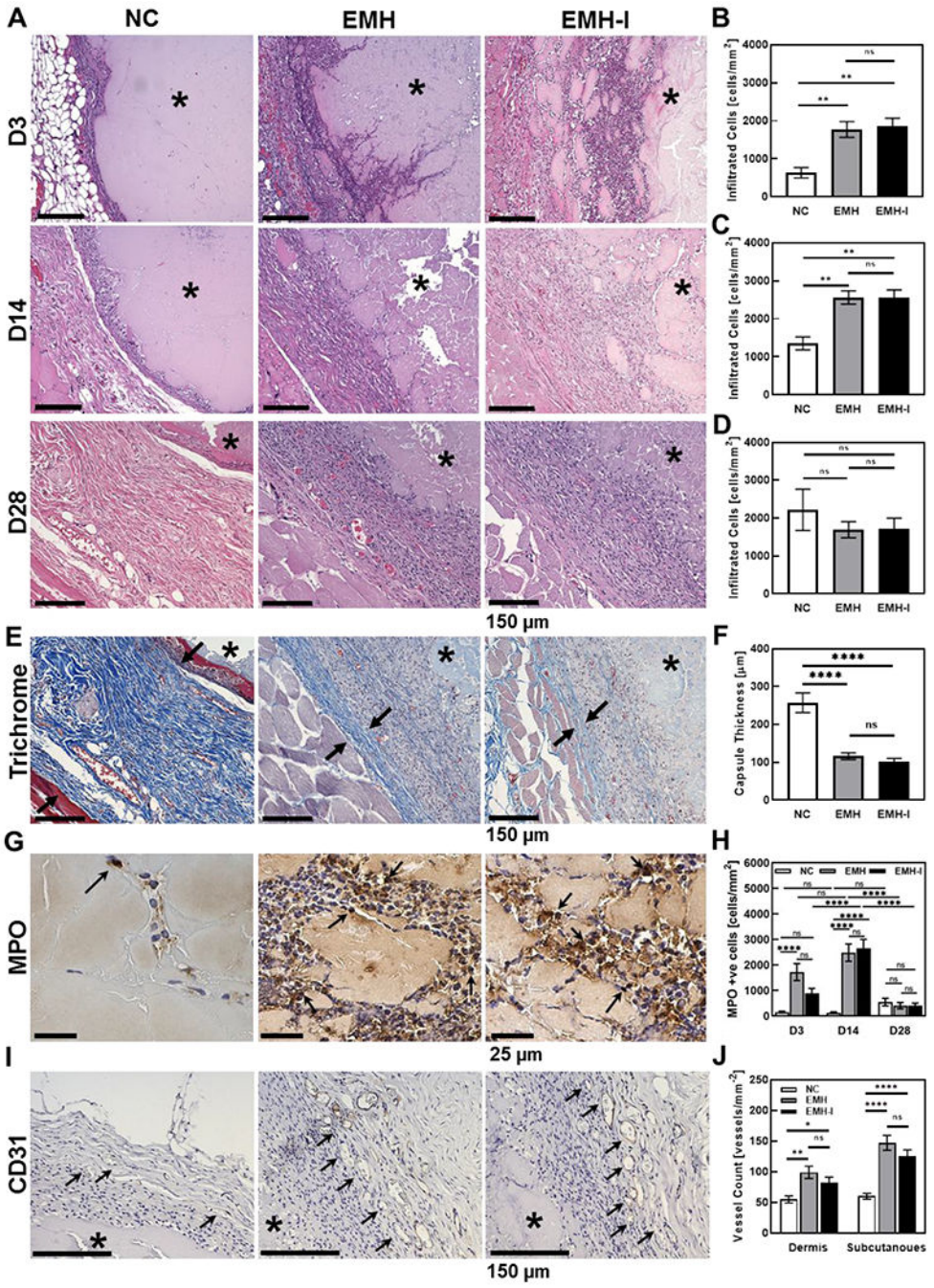


**Figure 3.**

Histological analysis of the gel specimens and surrounding tissues taken at different time points in rat subcutaneous injections. (A) Representative H&E stain of explanted NC, EMH and EMH-I at D3, D14, and D28 post subcutaneous injection. The total amount of infiltrated cells inside of the implanted region at (B) D3, (C) D14, and (D) D28 (n=4). (E) Representative Masson's Trichrome staining at 28 days. Black arrows show the fibrotic capsule. (F) Measured capsule thickness at D28 (n=8). Reduced capsule thickness formed around EMH and EMH-I compared to NC indicated better biocompatibility. (G)

Representative MPO immunostaining at D3. Black arrows point towards MPO positive cells. (H) Total amount of MPO in the implant area at D3, D14, and D28 showing subsided inflammatory responses of EMH and EMH-I over the long term (n=6). (I) Representative CD31 immunostaining at the gel-tissue interface at D28. Black arrows point towards CD31 positive blood vessels. (J) Amount of vessels at the dermis and subcutaneous sites at D28 showing pro-angiogenesis properties of EMH and EMH-I (n=4). The asterisks indicate the location of the injected material. One-way ANOVA tests were performed for statistical analysis. ns, not significant; *$p < 0.05$, **$p < 0.01$, ****$p < 0.0001$. Each data point represents average ± standard error.

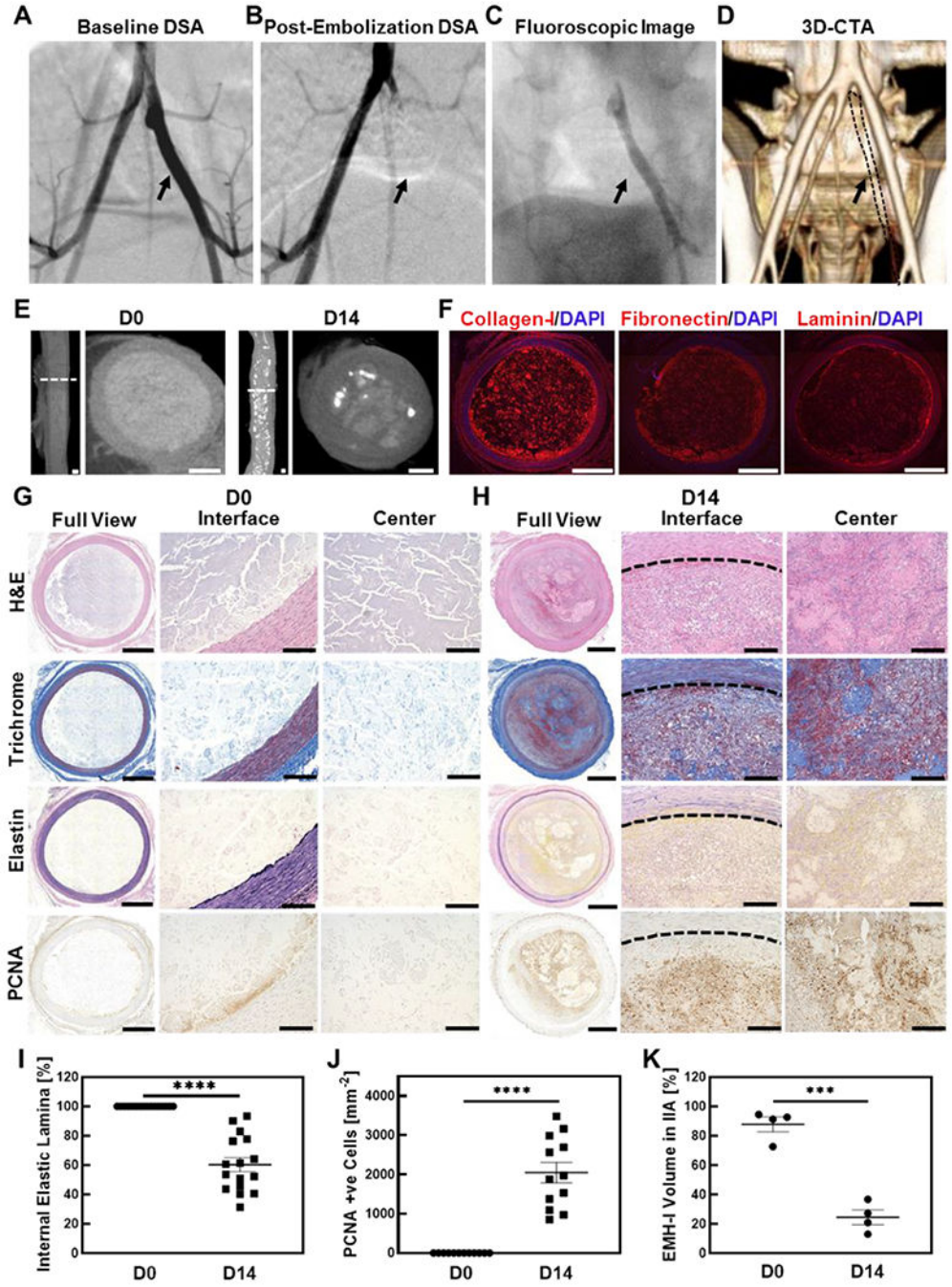


**Figure 4.**

Arterial embolization in a porcine model using EMH-I. Digitally subtracted angiography (DSA) of internal iliac artery (IIA) (A) before (arrow pointing the patent IIA), and (B) after embolization (arrow pointing embolized IIA with no flow). EMH-I is not visible in (B) because radiodense structures (such as bones and EMH-I) are digitally subtracted from the image in DSA, allowing clear visualization of patent blood vessels. Since IIA was occluded by EMH-I, it is not visualized on DSA. (C) Fluoroscopic image of EMH-I occluding IIA, showing its radiopacity and visibility (black arrow). (D) Reconstructed 3D CTA image

showing occluded IIA at D14. IIA is missing from 3D CTA since it is embolized and does not enhance (IIA outlined by black dot and pointed with black arrow) (E) Micro-CT images, both sagittal and transverse sectional views, of embolized IIA at D0 and D14. (F) Immunostaining of collagen-I, fibronectin, and laminin on embolized IIA at D0. Representative images of H&E, elastin, trichrome and PCNA staining of embolized IIA at (G) D0, and (H) D14 are shown. (I) Quantitative analysis of internal elastic lamina (n=4) showing reduction at D14. (J) PCNA positive cells in the lumen of the embolized artery were counted, showing a significant amount of proliferating cells in the lumen at D14 (n=4). (K) In vivo degradation profile of EMH-I volume inside of IIA obtained from microCT analysis. Bar scales for E and F are 1 mm, for full views in G and H are 1 mm, for interface and center images in G and H are 150 μm. ***$p < 0.005$, ****$p < 0.0001$. Each data point represents average ± standard error.

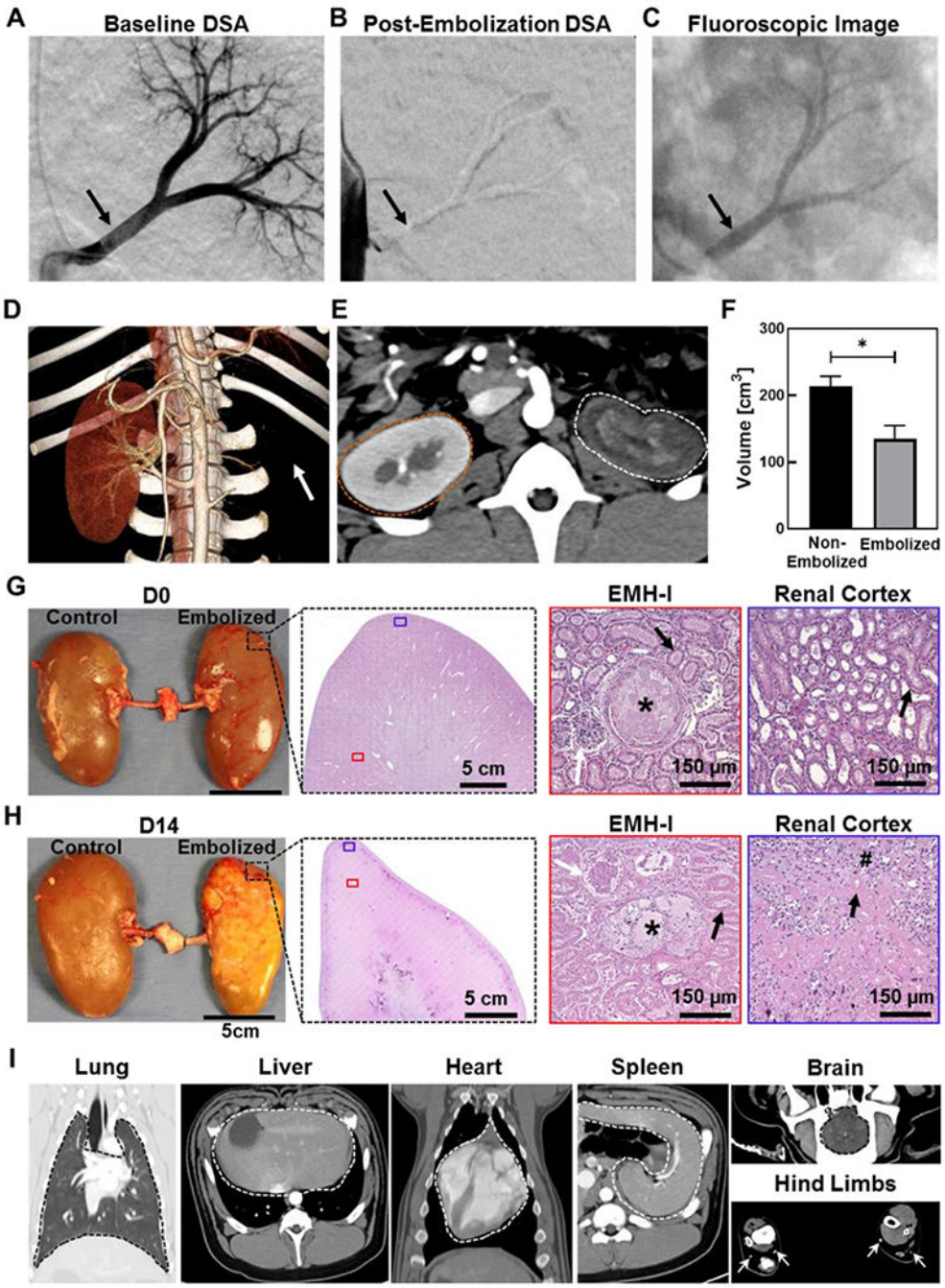


**Figure 5.**

Renal artery embolization in a porcine model using EMH-I. DSA of the left kidney (A) before (black arrow points to the patent main renal artery), and (B) after the delivery of EMH-I (black arrow points to the occluded main renal artery). EMH-I is not visible in (B) because radiodense structures (such as bones and EMH-I) are subtracted digitally from the image in DSA, allowing clear visualization of patent blood vessels. Since renal artery was occluded by EMH-I, it is not visualized on DSA. (C) Fluoroscopic image showing radiopaque EMH-I blocking the main renal artery as well as segmental arterial branches

(black arrow) in kidney. (D) 3D CTA image of non-embolized and embolized kidneys 14 days post-procedure. Embolized kidney is missing (location denoted by white arrow) due to the absence of blood flow and non-enhancement. (E) Axial CTA image showing the non-enhancing parenchyma of the embolized kidney (white dotted outline) compared to the control (orange dotted outline). (F) Volume of embolized kidney and non-treated kidney as determined by CTA (n=4). (G, H) Gross image of excised kidneys, and representative H&E images of embolized kidney showing EMH-I (asterisks) in embolized vessels and the renal cortex at D0, and fibrosis (hash sign) with loss of architecture at D14. White arrows pointed towards granuloma and black arrows showed tubules. (I) CT images of normal organs in animals that received EMH-I. Lung, liver, spleen, heart, and brain are outlined by dotted line. White arrows point to widely patent vessels in hind limbs showing no evidence for non-target embolization. $*p < 0.05$. Each data point represents average ± standard error.

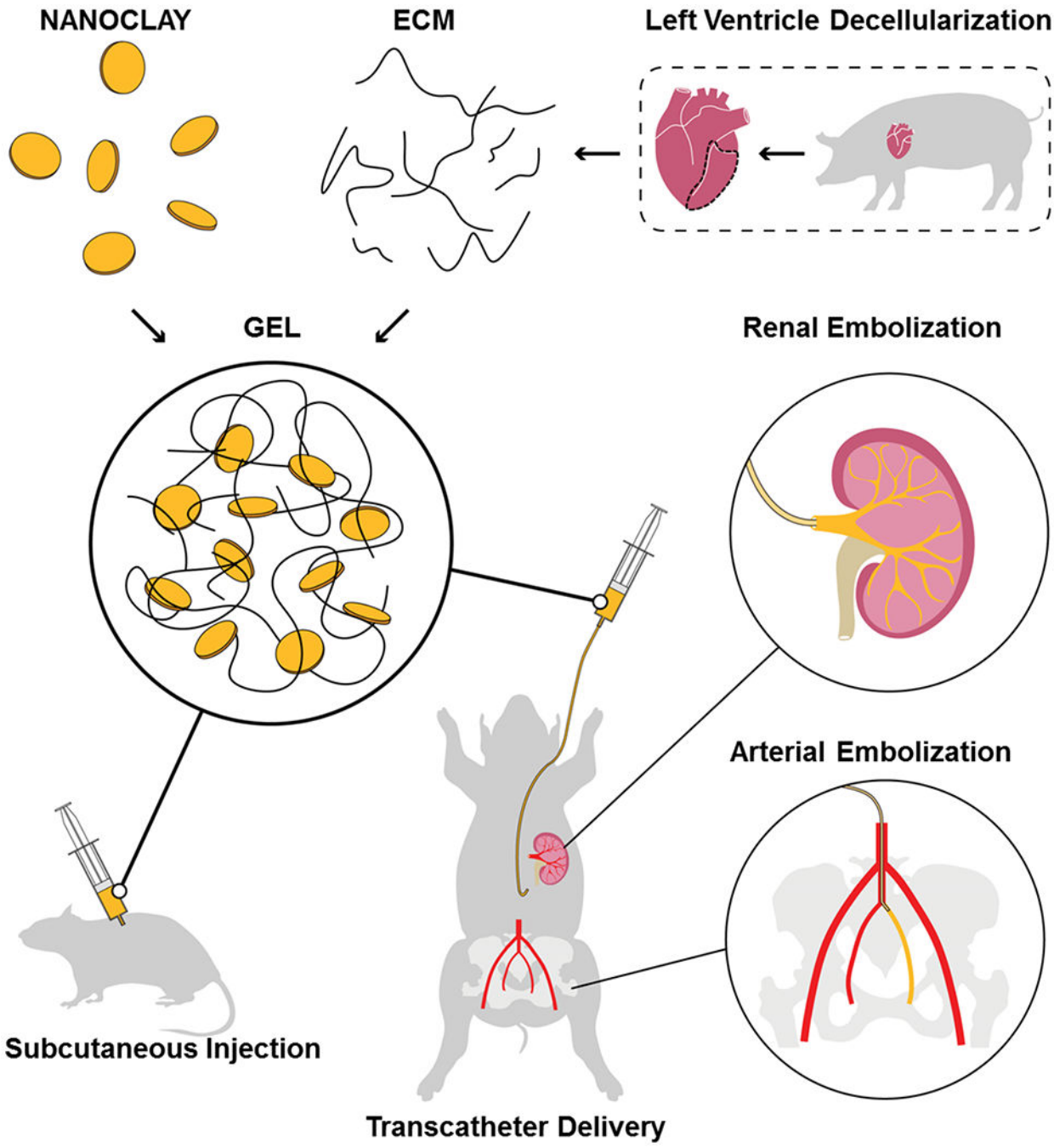


**Schematic 1.**

Schematics of ECM-NC nanocomposite gel fabrication and in vivo embolization testing. The black dotted line outlined the left ventricle of a porcine heart for decellularization.